

Origin of unexpected weak Gilbert damping in the LSMO/Pt bilayer system

Pritam Das¹, Pushpendra Gupta², Seung-Cheol Lee³, Subhankar Bedanta², and Satadeep Bhattacharjee^{1*}

¹ Indo-Korea Science and Technology Center (IKST), Bangalore, India

² National Institute of Science Education and Research, Bhubaneswar, India

³ Electronic Materials Research Center, Korea Institute of Science & Technology, Korea

We investigated the Gilbert damping in $\text{La}_{0.7}\text{Sr}_{0.3}\text{MnO}_3$ (LSMO) and $\text{La}_{0.7}\text{Sr}_{0.3}\text{MnO}_3/\text{Pt}$ (LSMO/Pt) heterostructures using first-principles calculations and Wannier interpolation techniques. Our work is motivated by recent experimental observations showing smaller Gilbert damping in LSMO/Pt films compared to their reference single-layer LSMO films, despite expectations of enhanced spin-pumping effects in the former. We analyze the electronic structures and transport behaviors, finding that LSMO thin films have a high spin Hall angle ($|\theta_{\text{SH}}|$). However, in LSMO/Pt, the presence of platinum significantly increases longitudinal conductivity, reducing $|\theta_{\text{SH}}|$. Despite the lower $|\theta_{\text{SH}}|$, LSMO/Pt shows a notable anti-damping contribution to Gilbert damping due to a larger spin diffusion length. In contrast, pure LSMO films with large $|\theta_{\text{SH}}|$ exhibit higher damping due to efficient spin-to-charge conversion via a self-induced inverse spin Hall effect (ISHE), as reported in a recent experiment. Finally, this work demonstrates that by fine-tuning the ratio of spin Hall conductivity to longitudinal charge conductivity, it is possible to engineer heterostructures with desired spin-to-charge or charge-to-spin conversion efficiencies even with weaker spin-orbit couplings.

In recent years, there has been a lot of interest in spintronic materials because of their potential applications in next-generation information storage and processing technology [1–3]. One of the most fascinating phenomena in this subject is the interplay of ferromagnetic and non-magnetic materials, which results in emergent effects including spin pumping and the inverse spin Hall effect (ISHE) [4–7]. The recent study by Gupta *et al.* observed the rare but significant coexistence of anti-damping and spin pumping in manganite and heavy metal heterostructures [8]. This experimental evidence of anti-damping and ISHE in the $\text{La}_{0.67}\text{Sr}_{0.33}\text{MnO}_3$ (LSMO)/Pt bilayer system advances our understanding of the intricate interactions between ferromagnets and heavy metals and sets the stage for theoretical investigations into the underlying mechanisms.

The LSMO/Pt bilayer system possesses unique properties due to its components. LSMO is a well-known colossal magnetoresistance material that exhibits ferromagnetic order with a high Curie temperature, making it an attractive choice for spin injection [9–11]. Platinum, on the other hand, is a heavy metal with strong spin-orbit coupling, which facilitates efficient spin-to-charge current conversion via the ISHE [12, 13]. The interaction of these materials in heterostructures provides an ideal environment for studying spin dynamics and spin-charge conversion. The simultaneous findings of anti-damping and the ISHE in this system indicate a complex interaction between spin pumping from the ferromagnetic LSMO layer and spin current absorption and conversion in the Pt layer [14].

Previous studies have shown that when a heavy metal (HM) is deposited adjacent to a ferromagnet (FM), the FM generates a spin current during spin pumping, which is dissipated in the HM. This spin current absorption in the HM leads to the relaxation of spins in the FM, thereby enhancing the effective

Gilbert damping. Factors such as proximity-induced magnetization in the HM, interface roughness, etc., can also enhance the damping in the system near the HM [15, 16]. This increased damping can limit the application of such devices in high-speed dynamics. However, there are instances where, instead of an enhancement, a reduction in effective damping, known as anti-damping, has been observed [8, 17]. Anti-damping, defined as the reduction in effective Gilbert damping in FM/HM bilayers compared to single FM films, suggests efficient spin injection and absorption at the interface, enabling the utilization of such devices without compromising their high-speed dynamical properties [18].

A comprehensive theoretical framework is required to clarify the microscopic mechanisms behind anti-damping events. Density Functional Theory (DFT) simulations are widely used for studying the electronic structure and spin-dependent interactions at the atomic level [19, 20]. DFT can help us understand the electrical conductivity and spin Hall conductivity of LSMO and Pt, as well as their interface. The efficiency of spin injection and subsequent spin-to-charge conversion processes are closely related to the electrical and spin Hall conductivities of the thin films. These computations can also provide insights into the role of interfacial states and the impact of structural and electronic features on observed spintronic phenomena.

In this work, we aim to bridge the gap between experimental observations and theoretical understanding of the LSMO/Pt bilayer system. By employing DFT calculations for LSMO, Pt, and LSMO/Pt heterostructures, we investigate their electrical and spin Hall conductivities. Additionally, to place our results in a broader context, we conduct a comparative study on the Co/Pt system, a benchmark for spin-pumping studies.

Our study demonstrates that the experimental observation of smaller damping in the Pt/LSMO system compared to pure LSMO can be explained by the significant reduction in the spin Hall angle (θ_{SH}). We show that in the Pt/LSMO system, the presence of the metallic Pt layer increases the longitudinal

* s.bhattacharjee@ikst.res.in

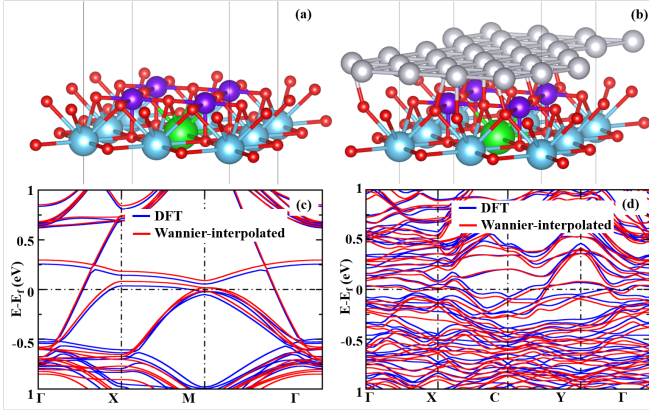


FIG. 1. Structural models and electronic band structures of LSMO and LSMO/Pt films. The top panel (a&b) corresponds to the structural models while bottom panels displays DFT band structure fitted with Wannier90 interpolated band structure for both LSMO (c) and LSMO/Pt (d).

conductivity (σ_{xx}), resulting in a much lower θ_{SH} . This substantial reduction in θ_{SH} decreases both the spin-orbit torque (SOT) antidamping effects and the damping effect due to the spin-pumping effect. However, the balance between the conversion from charge to spin (anti-damping) and spin to charge (damping) in this heterostructure leads to an overall smaller damping.

In contrast, the Co/Pt system exhibits a different behavior. The longitudinal conductivity and spin Hall conductivity in Co and Co/Pt do not show significant changes due to the addition of Pt. The spin Hall angle in Co/Pt is observed to be larger than in single Co films, indicating that the presence of Pt enhances the spin pumping effect and increases the Gilbert damping. This behavior is consistent with the well-known mechanisms in Co/Pt systems, where the enhanced spin current absorption in Pt leads to increased damping in the ferromagnetic layer.

Our findings indicate that the mechanisms responsible for the observed damping behavior in LSMO and LSMO/Pt do not appear in the Co and Co/Pt systems. In LSMO, the self-induced inverse spin Hall effect (ISHE) plays a crucial role, leading to higher damping due to efficient spin-to-charge conversion within the material. In LSMO/Pt, the interplay between the reduced θ_{SH} and the larger spin diffusion length results in a notable anti-damping contribution, balancing the overall damping. This intricate interplay of spin dynamics is not observed in Co/Pt, where the damping behavior is primarily governed by spin current absorption in the Pt layer.

To understand the relative magnitude of damping and anti-damping torques in LSMO and LSMO/Pt systems, we compared the spin Hall angles (θ_{SH}) in these two systems. The spin Hall angle is a crucial parameter that indicates the efficiency of the conversion from charge current to spin current, thereby influencing the strength of the spin pumping as well as spin-orbit torques [21]. It is important to note that recently Gupta *et al.* reported observation of a self-induced inverse spin Hall effect (ISHE) and spin pumping [22] within LSMO.

It can be noted that similar self-induced ISHE was observed by Tsukahara *et al.* [23] in permalloy at room temperature. This self-induced ISHE leads to the generation of a significant spin-pumping voltage within the LSMO film, indicating the presence of appreciable spin-to-charge conversion within the material. This finding is significant because it demonstrates a unique mechanism for spin current generation and spin-to-charge conversion that does not rely on spin currents generated in adjacent layers, as is typically seen in traditional measurement methods for the spin Hall effect.

The spin Hall angle is given by the following equation [24],

$$\theta_{SH} = \frac{2e}{\hbar} \frac{\sigma_{xy}^{SHC}}{\sigma_{xx}} \quad (1)$$

Where σ_{xy}^{SHC} is the spin Hall conductivity (SHC) and σ_{xx} is the longitudinal charge conductivity.

The intrinsic SHC was calculated by fitting DFT Hamiltonian to an effective Wannier Hamiltonian using Wannier90 approach and by using Kubo's formula [25],

$$\sigma_{xy}^{SHC} = -\frac{e^2}{\hbar} \frac{1}{VN} \sum_k \sum_n \Omega_{n,xy}(\mathbf{k}) f_{nk}. \quad (2)$$

The spin Berry curvature $\Omega_{n,xy}(\mathbf{k})$ can be obtained using the following equation [25]:

$$\Omega_{n,xy}(\mathbf{k}) = 2\hbar^2 \text{Im} \sum_{m \neq n} \frac{\langle nk | \hat{j}_x^s | mk \rangle \langle mk | -e\hat{v}_y | nk \rangle}{(\epsilon_{nk} - \epsilon_{mk})^2}, \quad (3)$$

Here \hat{j}_x^s is the spin current operator and is given by $\hat{j}_x^s = \frac{\hbar}{2} \{ \sigma_z, v_x \}$.

The ground state *ab initio* calculations were carried out in the framework of DFT implemented in the Vienna *ab initio* Simulation Package (VASP) [26]. The electronic band structure was calculated within the generalized gradient approximation (GGA) exchange-correlation functional of Perdew-Burke Ernzerhof (PBE) [27] with spin-orbit coupling (SOC) terms. All energies converged within a cutoff of 450 eV. The conjugate gradient algorithm was used for structural optimization. The convergence criteria for energy and force were 10^{-6} eV and 0.05 eV/Å, respectively. Once the ground state is obtained, the transport properties were calculated using the WANNIER90 package [28]. The longitudinal charge conductivity was calculated using the BOLTZWANN module [29]. To simulate the LSMO and LSMO/Pt films we considered the slab model as shown in Fig.1. The LSMO film was constructed with two monolayers of bulk LSMO (001) surface while LSMO/Pt film was constructed using the heterostructure of one monolayer of Pt (111) surfaces stacked on two monolayers of LSMO (001). A vacuum of 10Å was used. Dipole corrections were performed along the z-direction to eliminate the unwanted electric field effects.

Figures 1(b) and 1(d) present the electronic band structures of LSMO and LSMO/Pt, respectively. The band structures reveal that LSMO retains its metallic nature with bands crossing the Fermi level, while LSMO/Pt shows more complex band

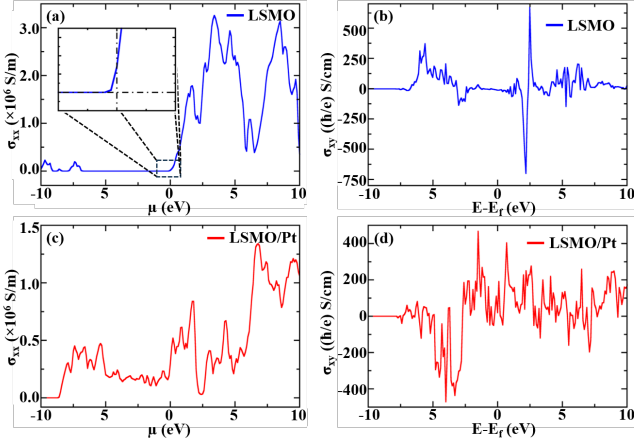


FIG. 2. The longitudinal charge conductivity and spin Hall conductivities. Upper panels (a&b):LSMO, lower panels (c&d): LSMO/Pt

hybridization due to the interaction with Pt layers. This hybridization can influence the spin-orbit coupling and subsequently the spin-Hall effect. The figure also demonstrates a successful Wannier interpolation in both cases.

The longitudinal conductivity (σ_{xx}) and spin Hall conductivity (σ_{xy}) for both systems are depicted in Figure 2. The σ_{xx} plots (Figures 2a and 2c) highlight a stark contrast between the two systems. For LSMO, the small longitudinal conductivity is observed at zero chemical potential ($\mu = 0$), indicating limited conducting channels. In contrast, the presence of Pt in LSMO/Pt significantly enhances σ_{xx} at zero chemical potential due to the additional pathways for charge transport which can be further understood from the Fig.1 where it is clear that Pt introduces additional states near Fermi energy facilitating better charge transport. As can be seen from the figure, the longitudinal conductivity (σ_{xx}) for LSMO is very small at $\mu = 0$ ($\sim 0.014 \times 10^6$ S/m), indicating poor charge transport properties near the Fermi level (E_F). This suggests a low density of states (DOS) at the Fermi level which is consistent with the electronic band structure shown in Fig.1 which depicts a single band crossing the Fermi level. However, it is important to note that at higher chemical potentials, LSMO has larger σ_{xx} . In principle, by doping to adjust the chemical potential, one can effectively tune the θ_{SH} in both LSMO and LSMO/Pt systems. It can be easily understood from the Fig.2 that n-type doping can reduce the θ_{SH} in LSMO further.

The spin Hall conductivities (σ_{xy}) for LSMO and LSMO/Pt (Figures 2b and 2d) further elucidate the spintronic properties. For LSMO, θ_{SH} is found to be -0.093 whereas for LSMO/Pt, it reduces to 0.007. This reduction is primarily attributed to the increased longitudinal conductivity (which is in the denominator of Eq.1) in LSMO/Pt due to Pt bands crossing the Fermi energy, which dilutes the effective spin Hall efficiency. The observed Gilbert damping in LSMO is larger than in LSMO/Pt, which can be rationalized by considering the details of the spin-orbit torque mechanisms: As mentioned before, in LSMO there is evidence of a self-induced ISHE, where the material itself generates a transverse charge current from an internal spin current without the need for an exter-

nal interface. In this case, the absence of an external interface means there is no anti-damping mechanism from an external source (due to the injection of spin current from another material). The self-induced spin pumping effect powered by larger values of $|\theta_{SH}|$ in LSMO, therefore, leads to significant angular momentum dissipation within the material itself, contributing to larger effective damping via conversion of spin current to charge current through $\mathbf{J}_c = \theta_{SH} \left(\frac{\hbar}{2e} \right) (\mathbf{J}_s \times \boldsymbol{\sigma})$. Here \mathbf{J}_c and \mathbf{J}_s are respectively charge and spin current density. $\boldsymbol{\sigma}$ is the direction of the spin polarization [30].

Another important point we can gather from the sign of the spin Hall angle we have computed. The sign of θ_{SH} determines the direction of the charge current generated by the ISHE. It can be seen that θ_{SH} for LSMO is negative. However, the absolute value $|\theta_{SH}|$ indicates the strength of the spin-to-charge conversion. Thus, a large $|\theta_{SH}|$ (regardless of whether θ_{SH} is positive or negative) can result in a significant ISHE. Recently, Bleser *et al.* [31] demonstrated large spin-to-charge conversion with a negative spin Hall angle in thermally evaporated chromium thin films. The effective sign of θ_{SH} can also be influenced by the thickness of the film. The difference in the composition between the MnO_2 and $(\text{La,Sr})\text{O}$ layers in the structural model we considered (see Fig.1) therefore induces a strong SOC at the interface. This gradient can enhance the ISHE in a manner similar to FePt films as seen in recent experiments [32].

In the LSMO/Pt heterostructure, on the other hand, the presence of SHE guarantees the presence of ISHE as well. The ISHE contributes to spin pumping, where spin currents from LSMO are absorbed by Pt, leading to angular momentum dissipation as mentioned above which contributes to the overall damping in addition to the intrinsic damping. The SHE in Pt generates spin currents in response to an applied charge current is given by $\mathbf{J}_s = \theta_{SH} \left(\frac{2e}{\hbar} \right) (\mathbf{J}_c \times \boldsymbol{\sigma})$ which can flow back into LSMO and exert anti-damping torques. The presence of both mechanisms therefore compete here and balances the overall damping in the LSMO/Pt heterostructure. From the seminal work of Haney *et al.* [33], it can be seen that, the anti-damping torque,

$$\tau_{ad} \propto \theta_{SH} \frac{\left(1 - e^{-t_{HM}/\lambda_{sf}} \right)^2}{1 + e^{-2t_{HM}/\lambda_{sf}}} \quad (4)$$

A small value of θ_{SH} implies a less efficient spin-to-charge conversion, which directly reduces τ_{ad} . However, in the experiment, an antidamping torque is still seen [8]. This can be attributed to the larger spin diffusion length present in the system. A larger spin diffusion length (λ_{sf}) means that the spin polarization decays slowly, which makes the generated spin current reach the ferromagnetic easily. The term $(1 - e^{-t_{HM}/\lambda_{sf}})$ will be larger, as $e^{-t_{HM}/\lambda_{sf}}$ will decay slowly, t_{HM} being the thickness of the heavy metal layers. It is to be noted that materials like permalloy have been reported with a relatively smaller value of θ_{SH} with λ_{sf} of around 7.0 nm [34]. This indicates that while the θ_{SH} is relatively low, the λ_{sf} is sufficiently large, allowing for effective spin transport. Also, Fache *et al* reported that for CoFeB/Ir heterostructure,

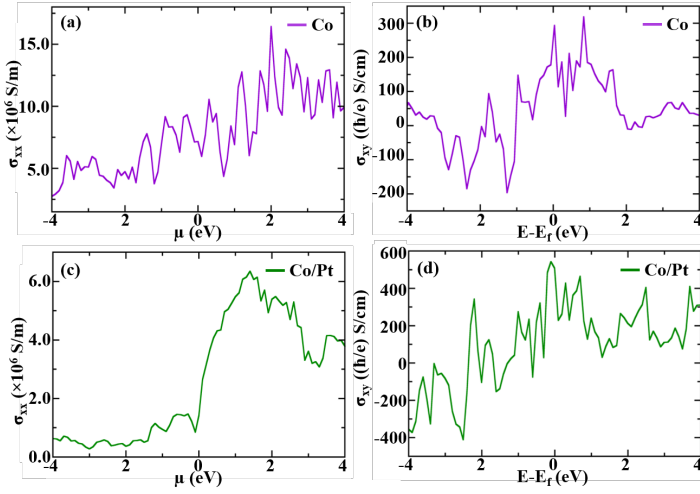


FIG. 3. The longitudinal charge conductivity and spin Hall conductivities. Upper panels (a&b):Co, lower panels (c&d): Co/Pt

Ir showed a non-negligible spin diffusion length of 1.3 nm in spite of the fact that θ_{SH} for the Ir is only 0.2 times that of Pt [35].

To understand how the spin-diffusion length behaves in the LSMO/Pt system, we considered two monolayers of LSMO and four monolayers of Pt as shown in Fig.4. We obtained the layer-resolved spin polarization using spin-polarized DFT calculations, which provided the input data for spin polarization as a function of distance. The layer-resolved spin polarization was obtained by the equation given by [36],

$$P_L = \frac{D_L^\uparrow(E_F) - D_L^\downarrow(E_F)}{D_L^\uparrow(E_F) + D_L^\downarrow(E_F)} \quad (5)$$

Here L is the layer index and $D_L^{\uparrow(\downarrow)}(E_F)$ is the density of states at the Fermi energy for the majority (minority) spin electrons. By fitting these data points to an exponential decay model, $P(z) = P_0 \exp(-z/\lambda_{sf}) + C$, with the initial spin polarization P_0 to be close to 1.0, we determined the spin diffusion length (λ_{sf}). The fitting process yielded a spin diffusion length of $\lambda_{sf} \approx 21.75 \text{ \AA}$. Converting this to nanometers (nm), we found $\lambda_{sf} = 2.175 \text{ nm}$. As one can see this value is quite significant, this can support the anti-damping torque as mentioned above (even with a relatively small value of θ_{SH}).

Finally, to demonstrate that these results are an exception and not generally expected, we performed similar calculations for the Co/Pt system. The interface was considered using one monolayer of Co and one monolayer of Pt. The observed $\theta_{SH} = 0.036$ for the Co/Pt bilayer system is larger than the case of a single Co-monolayer for which a quite relatively smaller value of $\theta_{SH} = 0.004$ is observed. The stronger θ_{SH} in this heterostructure suggests that the Gilbert damping would increase with increasing Pt thickness due to enhanced spin pumping effect as for example reported by Mahfouzi *et al.* [37]. As seen from Fig.3, the Co/Pt interface has smaller longitudinal conductivity and higher SHC in comparison to the Co mono-layer something opposite in nature if one com-

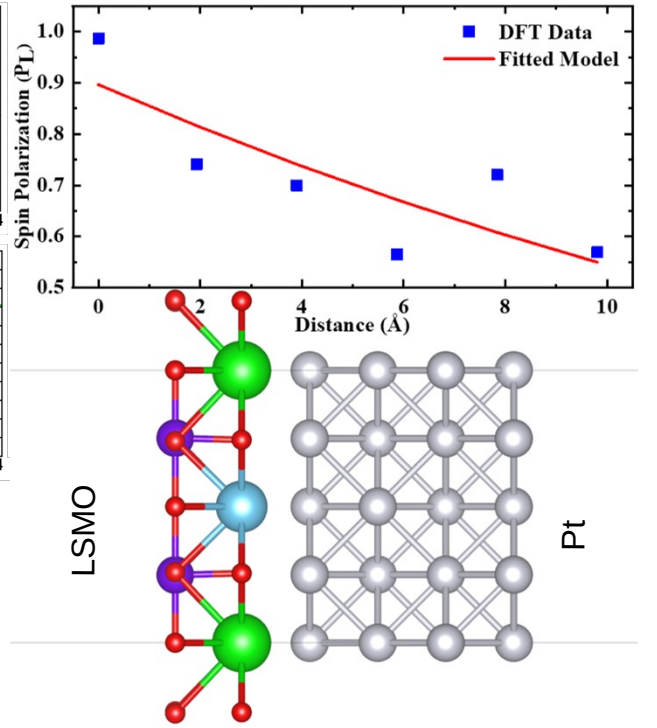


FIG. 4. Layer dependent spin polarization of the LSMO/Pt heterostructure obtained using Eq.5.

pares with LSMO and LSMO/Pt heterostructure. It should be noted here that LSMO being a half-metal should have smaller intrinsic Gilbert damping as can be understood either from Kambersky's torque-torque model [38, 39] or from the work of Gilmore *et al.* [40]. As LSMO is half metal, there is no spin-flip scattering for the minority spin electrons due to the reduction in the available states, which leads to fewer scattering events that contribute to energy dissipation, thereby reducing the damping. Therefore appearance of a relatively larger damping in LSMO films can be easily rationalized by self-induced ISHE.

It is worth noting that, although self-induced ISHE is prominent in the experiment if the self-induced ISHE seen in LSMO is associated with MnO_2 layers as the source of spin current and (La, Sr)O layers as the source of spin-orbit interaction, it also necessitates considering the inverse effect, namely the anti-damping torque due to the intrinsic SHE in the (La, Sr)O layer and the generation of spin current. It can be argued here that in ultrathin layers, the anti-damping torque, often associated with the SHE in the heavy metal, might be suppressed due to the reduced spin diffusion length in very thin HM layers. The spin current generated by SHE may not effectively reach the FM layer to induce significant anti-damping torque, especially if the thickness of the HM layer is less than the spin diffusion length. It can be noted that while a shorter spin diffusion length supports the spin-pumping via ISHE (as demonstrated by [35] that CoFeB/Ir with spin diffusion length of 1.3 nm has higher spin pumping effect in comparison to CoFeB/Pt with a larger spin diffusion length of 2.6 nm) as spin currents

are absorbed more effectively near the interface between the ferromagnet and the non-magnetic layer, the longer spin diffusion lengths are better suited for generating effective spin-orbit torques. Another possible contribution to the absence of such an effect in the experiment could come from the magnetic moment. The anti-damping torque due to the SHE effect scales as $\frac{1}{M_s^2}$ [41], while the ISHE scales as $\frac{1}{M_s}$ [32]. From our DFT calculations, we find the value of M_s for LSMO and LSMO/Pt films to be $8.3\mu_B$ and $7.02\mu_B$, respectively. Finally, the efficiency parameter [41] might be small for LSMO.

In summary, the interplay between intrinsic damping mechanisms, spin pumping, and anti-damping torques in FM/HM bilayers presents a rich landscape for theoretical and experimental exploration. Our findings suggest that tailoring the interface properties and electronic structure can significantly impact the damping behavior, offering pathways to optimize materials for spintronic applications. Particularly, this study

highlights that it is feasible to engineer materials with desired spin Hall angles (θ_{SH}) even in cases where the intrinsic spin-orbit coupling is not prominently strong. This can be achieved by fine-tuning the ratio of spin Hall conductivity (SHC) to longitudinal charge conductivity. By optimizing this ratio, one can effectively control the spin Hall angle, thereby modulating the efficiency of spin-to-charge conversion and the associated damping properties. Future studies could investigate the impact of varying the thickness of the Pt layer, introducing different heavy metals with varying spin-orbit coupling strengths, or applying external fields to modulate the spin dynamics. Understanding the role of temperature and external stress on damping parameters could also provide valuable insights for practical applications.

This work was supported by the Korea Institute of Science and Technology, GKP (Global Knowledge Platform, Grant number 2V6760) project of the Ministry of Science, ICT and Future Planning.

-
- [1] S. D. Bader and S. S. P. Parkin, *Annual Review of Condensed Matter Physics* **1**, 71 (2010).
- [2] I. Žutić, J. Fabian, and S. D. Sarma, *Rev. Mod. Phys.* **76** (2004).
- [3] S. A. Wolf, D. D. Awschalom, R. A. Buhrman, J. M. Daughton, S. von Molnár, M. L. Roukes, A. Y. Chtchelkanova, and D. M. Treger, *Science* **294** (2001).
- [4] E. Saitoh, M. Ueda, H. Miyajima, and G. Tatara, *Appl. Phys. Lett.* **88** (2006).
- [5] Y. Kajiwara *et al.*, *Nature* **464** (2010).
- [6] S. Bhattacharjee, S. Singh, D. Wang, M. Viret, and L. Bellaiche, *Journal of Physics: Condensed Matter* **26**, 315008 (2014).
- [7] K. Ando, S. Takahashi, J. Ieda, Y. Kajiwara, H. Nakayama, T. Yoshino, K. Harii, Y. Fujikawa, M. Matsuo, S. Maekawa, *et al.*, *Journal of applied physics* **109** (2011).
- [8] P. Gupta, B. B. Singh, K. Roy, A. Sarkar, M. Waschke, T. Brueckel, and S. Bedanta, *Nanoscale* **13** (2021).
- [9] A. de Andrés, J. Rubio, G. Castro, S. Taboada, J. M. Colino, *Appl. Phys. Lett.* **83** (2003).
- [10] A. Urushibara, Y. Moritomo, T. Arima, A. Asamitsu, G. Kido, and Y. Tokura, *Phys. Rev. B* **51**, 14103 (1995).
- [11] J.-H. Park, E. Vescovo, H.-J. Kim, C. Kwon, R. Ramesh, and T. Venkatesan, *Nature* **392** (1998).
- [12] E. Sagasta, Y. Omori, M. Isasa, M. Gradhand, L. E. Hueso, Y. Niimi, Y. Otani, and F. Casanova, *Phys. Rev. B* **94** (2016).
- [13] A. Hoffmann, *IEEE Transactions on Magnetics* **49** (2013).
- [14] S. Y. Huang, X. Fan, D. Qu, Y. P. Chen, W. G. Wang, J. Wu, T. Y. Chen, J. Q. Xiao, and C. L. Chien, *Phys. Rev. Lett.* **109**, 107204 (2012).
- [15] C. Swindells, H. Głowiński, Y. Choi, D. Haskel, P. P. Michałowski, T. Hase, F. Stobiecki, P. Kuświk, and D. Atkinson, *Phys. Rev. B* **105**, 094433 (2022).
- [16] C. Swindells, H. Głowiński, Y. Choi, D. Haskel, P. P. Michałowski, T. Hase, P. Kuświk, and D. Atkinson, *Applied Physics Letters* **119**, 152401 (2021).
- [17] N. Behera, S. Chaudhary, and D. K. Pandya, *Sci Rep* **6**, 1 (2016).
- [18] D. M. Lattery, D. Zhang, J. Zhu, X. Hang, J.-P. Wang, and X. Wang, *Sci Rep* **8**, 13395 (2018).
- [19] Y. Tserkovnyak, A. Brataas, and G. E. W. Bauer, *Phys. Rev. Lett.* **88** (2002).
- [20] Y. Tserkovnyak, A. Brataas, G. E. W. Bauer, and B. I. Halperin, *Rev. Mod. Phys.* **77** (2005).
- [21] E. Ketkar, G. K. Shukla, S.-C. Lee, S. Bhattacharjee, and S. Singh, *Applied Physics Letters* **123** (2023).
- [22] P. Gupta, I. J. Park, A. Swain, A. Mishra, V. P. Amin, and S. Bedanta, *Physical Review B* **109**, 014437 (2024).
- [23] A. Tsukahara, Y. Ando, Y. Kitamura, H. Emoto, E. Shikoh, M. P. Delmo, T. Shinjo, and M. Shiraishi, *Physical Review B* **89**, 235317 (2014).
- [24] D. Qu, S.-Y. Huang, B. Miao, S. Huang, and C. Chien, *Physical Review B* **89**, 140407 (2014).
- [25] J. Qiao, J. Zhou, Z. Yuan, and W. Zhao, *Physical Review B* **98**, 214402 (2018).
- [26] G. Kresse and J. Furthmüller, *Computational Materials Science* **6**, 15 (1996).
- [27] J. P. Perdew, K. Burke, and M. Ernzerhof, *Physical Review Letters* **77**, 3865 (1996).
- [28] G. Pizzi, V. Vitale, R. Arita, S. Blügel, F. Freimuth, G. Géranton, M. Gibertini, D. Gresch, C. Johnson, T. Koretsune, *et al.*, *Journal of Physics: Condensed Matter* **32**, 165902 (2020).
- [29] G. Pizzi, D. Volja, B. Kozinsky, M. Fornari, and N. Marzari, *Computer Physics Communications* **185**, 422 (2014).
- [30] E. Saitoh, M. Ueda, H. Miyajima, and G. Tatara, *Applied physics letters* **88** (2006).
- [31] S. Bleser, R. Greening, M. Roos, L. Hernandez, X. Fan, and B. Zink, *Journal of Applied Physics* **131** (2022).
- [32] J. Ampuero, A. Anadón, H. Damas, J. Ghanbaja, S. Petit-Watlot, J.-C. Rojas-Sánchez, D. V. Rodriguez, J. Gómez, A. Butera, and L. Avilés-Félix, *arXiv preprint arXiv:2405.11948* (2024).
- [33] P. M. Haney, H.-W. Lee, K.-J. Lee, A. Manchon, and M. D. Stiles, *Physical Review B—Condensed Matter and Materials Physics* **87**, 174411 (2013).
- [34] Y.-H. Huang, Y.-C. Weng, C.-T. Liang, and J. Lin, *AIP Advances* **10** (2020).
- [35] T. Fache, J. Rojas-Sanchez, L. Badie, S. Mangin, and S. Petit-Watlot, *Physical Review B* **102**, 064425 (2020).
- [36] S. Bhattacharjee and S.-C. Lee, *Scientific Reports* **9**, 8381 (2019).

- [37] F. Mahfouzi, J. Kim, and N. Kioussis, *Physical Review B* **96**, 214421 (2017).
- [38] V. Kamberský, *Physical Review B—Condensed Matter and Materials Physics* **76**, 134416 (2007).
- [39] C. Liu, C. K. Mewes, M. Chshiev, T. Mewes, and W. H. Butler, *Applied Physics Letters* **95** (2009).
- [40] K. Gilmore, Y. Idzerda, and M. D. Stiles, *Physical review letters* **99**, 027204 (2007).
- [41] J. Sinova, S. O. Valenzuela, J. Wunderlich, C. Back, and T. Jungwirth, *Reviews of modern physics* **87**, 1213 (2015).